Phyllosilicate Diversity and Past Aqueous Activity Revealed at Mawrth Vallis, Mars

Janice L. Bishop, *et al.*

Science **321**, 830 (2008);
DOI: 10.1126/science.1159699

The energetic locations of the 3s Rydberg and $\pi^* \leftarrow n$ manifolds in the cation Franck-Condon region correlate well with the KER range over which each Dalitz feature was observed (Fig. 4). The maximum observed KER of 5 eV associated with the acute feature is close to the vertical energy for the Rydberg states (i.e., 5.17 and 5.11 eV above the 3HCN limit for the singlet and triplet, respectively). The maximum observed KER of 4 eV for symmetric dissociation lies 0.33 eV higher in energy than the vertical energy of the highest $\pi^* \leftarrow n$ state, $^1A_2$, which is located at 3.67 eV above the 3HCN limit and has D_{3h} equilibrium structure. The small separation between singlet and triplet states does not allow us to discriminate between these manifolds. However, the three-fold degeneracy of the triplets might lead one to expect triplets to be populated more frequently. On the other hand, the rate of electronic relaxation to the ground-state singlet PES is likely to be much slower for the triplets.

Nonadiabatic processes that span multiple electronic states are ubiquitous in the chemistry of energetic molecules and play a notable role in many types of natural phenomena (e.g., in biological, atmospheric, and combustion chemistry). The interactions between different electronic states are important even for reactions proceeding on a single PES, as reaction barriers can often be explained in terms of coupled diabatic states correlating with the reactants and the products. Our results show the progress being made toward analytical approaches to understanding the complexities of larger molecules.

In a broader context, this work raises a number of fundamental questions: How common is it for the equilibrium structure of an excited electronic state to determine the outcome of a reaction proceeding on another surface, and to what extent can the reflection principle be applied to polyatomic systems? With how much confidence can one rely on electronic couplings when considering the possible pathways of a nonadiabatic process? Would the difference between conical and glancing intersections manifest itself so prominently in molecules with lower symmetry? These questions all warrant future study. Our results show that synergism between theory and experiment can lead to greater understanding of how nonadiabatic behavior plays a role in these complicated systems.

References and Notes

1. C. Maul, K. H. Gericke, *Int. Rev. Phys. Chem.* **16**, 1 (1997).
2. Y. Osamura, H. F. Schaefer, M. Dupuis, W. A. Lester, *J. Chem. Phys.* **75**, 5828 (1981).
3. J. Guenther, D. Krankowsky, K. Mauersberger, *Chem. Phys. Lett.* **324**, 31 (2000).
4. G. S. Ondrey, R. Bersohn, *J. Chem. Phys.* **81**, 4517 (1984).
5. T. Gejo, J. A. Harrison, J. R. Huber, *J. Phys. Chem.* **100**, 13941 (1996).
6. Y. A. Dyakov *et al.*, *J. Phys. Chem. A* **111**, 9591 (2007).
7. J. Lee *et al.*, *Phys. Chem. Chem. Phys.* **6**, 945 (2004).
8. S. V. Pai, C. F. Chabalowski, B. M. Rice, *J. Phys. Chem.* **100**, 5681 (1996).
9. Y. Osamura, M. Unno, K. Hashimoto, *J. Am. Chem. Soc.* **109**, 1370 (1987).
10. R. E. Continetti, *Annu. Rev. Phys. Chem.* **52**, 165 (2001).
11. See supporting material on *Science* Online.
12. L. Kolaitis, D. M. Lubman, *Anal. Chem.* **58**, 1993 (1986).
13. H. Kato, K. Hirao, K. Yamashita, *J. Mol. Struct. (Theochem)* **88**, 265 (1982).
14. A. Salop, D. C. Lorents, J. R. Peterson, *J. Chem. Phys.* **54**, 1187 (1971).
15. V. Sidis, *J. Phys. Chem.* **93**, 8128 (1989).
16. C. M. Laperle, J. E. Mann, T. G. Clements, R. E. Continetti, *Phys. Rev. Lett.* **93**, 153202 (2004).
17. U. Galster, F. Baumgartner, U. Müller, H. Helm, M. Jungen, *Phys. Rev. A* **72**, 062506 (2005).
18. R. H. Dalitz, *Philos. Mag.* **44**, 1068 (1953).
19. C. Fridh, L. Asbrink, B. O. Jonsson, E. Lindholm, *Int. J. Mass Spectrom. Ion Phys.* **8**, 85 (1972).
20. K. K. Innes, I. G. Ross, W. R. Moomaw, *J. Mol. Spectrosc.* **132**, 492 (1988).
21. A. B. J. Parusel, G. Kohler, H. Nooijen, *J. Phys. Chem. A* **103**, 4056 (1999).
22. J. F. Stanton, R. J. Bartlett, *J. Chem. Phys.* **98**, 7029 (1993).
23. H. Koch, O. Christiansen, P. Jorgensen, J. Olsen, *Chem. Phys. Lett.* **244**, 75 (1995).
24. A. I. Krylov, *Annu. Rev. Phys. Chem.* **59**, 433 (2008).
25. Y. N. Demkov, *Sov. Phys. JETP* **18**, 138 (1964).
26. R. J. Cave, M. D. Newton, *Chem. Phys. Lett.* **249**, 15 (1996).
27. R. Schinke, *Photodissociation Dynamics* (Cambridge Univ. Press, Cambridge, 1993), pp. 109–133.
28. V. A. Mozhayskiy, D. Babikov, A. I. Krylov, *J. Chem. Phys.* **124**, 224309 (2006).
29. J. J. Dillon, D. R. Yarkony, *J. Chem. Phys.* **126**, 124113 (2007).

30. Supported by U.S. Air Force Office of Scientific Research grant FA9550-04-1-0035 (J.D.S., J.E.M., and R.E.C.) and NSF grant CHE-0616271 (V.M. and A.I.K.). This work was conducted under the auspices of the iOpenShell Center for Computational Studies of Electronic Structure and Spectroscopy of Open-Shell and Electronically Excited Species, supported by NSF through Chemistry Research Instrumentation and Facilities Cyberinfrastructure and Research Facilities Program (CRIF:CRF) grants CHE-0625419, CHE-0624602, and CHE-0625237.

Supporting Online Material

www.sciencemag.org/cgi/content/full/321/5890/826/DC1
Materials and Methods
Figs. S1 to S10
Tables S1 to S5
References

11 March 2008; accepted 23 June 2008
10.1126/science.1157617

Phyllosilicate Diversity and Past Aqueous Activity Revealed at Mawrth Vallis, Mars

Janice L. Bishop,[1]* Eldar Z. Noe Dobrea,[2] Nancy K. McKeown,[3] Mario Parente,[4] Bethany L. Ehlmann,[5] Joseph R. Michalski,[6] Ralph E. Milliken,[2] Francois Poulet,[6] Gregg A. Swayze,[7] John F. Mustard,[5] Scott L. Murchie,[8] Jean-Pierre Bibring[6]

Observations by the Mars Reconnaissance Orbiter/Compact Reconnaissance Imaging Spectrometer for Mars in the Mawrth Vallis region show several phyllosilicate species, indicating a wide range of past aqueous activity. Iron/magnesium (Fe/Mg)–smectite is observed in light-toned outcrops that probably formed via aqueous alteration of basalt of the ancient cratered terrain. This unit is overlain by rocks rich in hydrated silica, montmorillonite, and kaolinite that may have formed via subsequent leaching of Fe and Mg through extended aqueous events or a change in aqueous chemistry. A spectral feature attributed to an Fe^{2+} phase is present in many locations in the Mawrth Vallis region at the transition from Fe/Mg-smectite to aluminum/silicon (Al/Si)–rich units. Fe^{2+}-bearing materials in terrestrial sediments are typically associated with microorganisms or changes in pH or cations and could be explained here by hydrothermal activity. The stratigraphy of Fe/Mg-smectite overlain by a ferrous phase, hydrated silica, and then Al-phyllosilicates implies a complex aqueous history.

The Mawrth Vallis outflow channel (~25°N, 20°W) cuts through the ancient cratered Noachian highland terrain near the border with the lowlands. A variety of rocks are exposed that reveal the early aqueous history of the planet. Indurated light-toned units with complex spatial and stratigraphic relations are overlain by a darker, more heavily cratered material. Erosion in many locations exposes phyllosilicate-bearing outcrop within the light-toned rocks (*1*). Here we describe the specific clay minerals identified.

Hyperspectral images acquired by the Compact Reconnaissance Imaging Spectrometer for Mars (CRISM) (*2*, *3*) exhibit a variety of signatures in the visible/near-infrared (VNIR: ~0.4 to 4 μm) that are attributed to phyllosilicates and are consistent with observations of this area made by the Observatoire pour la Minéralogie, l'Eau, les Glaces et l'Activité (OMEGA) instrument on Mars Express (*3*–*5*). OMEGA data revealed the presence of montmorillonite and nontronite based on Al-OH and Fe-OH absorption bands near 2.2 and 2.3 μm, respectively (*4*, *6*). OMEGA data (Fig. 1) show Fe/Mg-phyllosilicates near the outflow channel and in a few other large outcrops observable at

[1]SETI Institute and NASA Ames Research Center, Mountain View, CA 94043, USA. [2]Jet Propulsion Laboratory, California Institute of Technology, Pasadena, CA 91109, USA. [3]Department of Earth and Planetary Sciences, University of California Santa Cruz, Santa Cruz, CA 95064, USA. [4]Department of Electrical Engineering, Stanford University, Stanford, CA 94305, USA. [5]Department of Geological Sciences, Brown University, Providence, RI 02912, USA. [6]Institut d'Astrophysique Spatiale, Orsay, 91405, France. [7]U.S. Geological Survey, Denver, CO 80225, USA. [8]Johns Hopkins University Applied Physics Laboratory, Laurel, MD 20723, USA.

*To whom correspondence should be addressed. E-mail: jbishop@seti.org

a resolution of hundreds of meters per pixel. Al-phyllosilicates and/or hydrated silica (not distinguished in Fig. 1) are associated with many Fe/Mg-phyllosilicate outcrops. We used the increased spatial and spectral resolution of CRISM data to more precisely identify the types of phyllosilicates present, to map them on a finer scale, and to determine their stratigraphic relationships (*7*).

CRISM spectra (Fig. 2) in the western part of Mawrth Vallis, where an areally extensive (>10 km) exposure of phyllosilicate-bearing units is observed, exhibit bands at ~1.4, 1.92, 2.30, and 2.39 μm (Fig. 2A, spectra c and d; Fig. 3B, spectra e, g, and h). The 2.30- and 2.39-μm bands lie in between the band centers observed for the Fe-smectite nontronite and the Mg-smectite hectorite (*3*, *8*) and are thus attributed to smectite having both Fe and Mg in octahedral sites such as Mg-bearing nontronite. An upward slope from ~1 to 1.5 μm is abundant in rocks surrounding the main exposure of the Fe/Mg-smectite (Fig. 2A, spectrum e; Fig. 3B, spectrum f) and is consistent with an Fe^{2+}-bearing phase such as a ferrous clay. Other spectra at higher elevations around the Fe/Mg-smectite exhibit bands near 1.4, 1.92, and 2.21 μm (Fig. 2A, spectrum g; Fig. 3A, spectrum a) that are consistent with the Al-smectite montmorillonite (*9*). Similar spectra having broad features near 2.18 to 2.26 μm

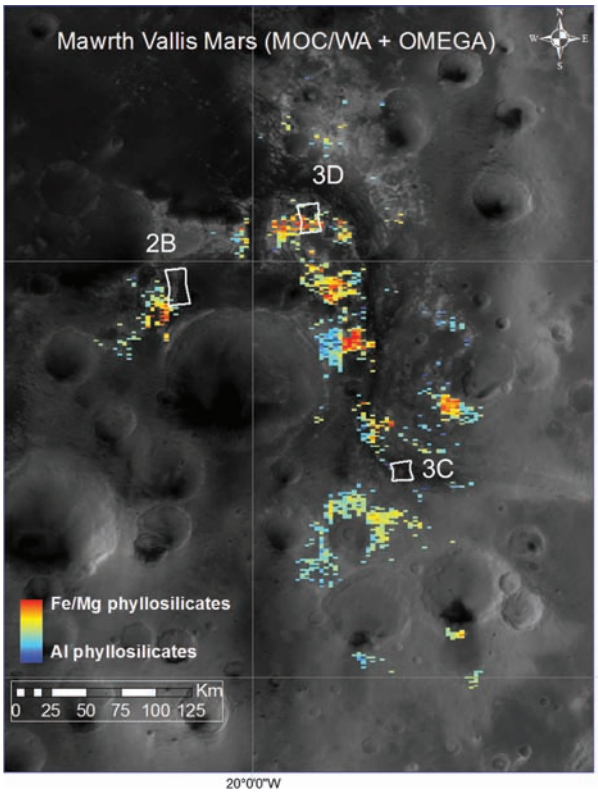

Fig. 1. Mars Orbiter Camera wide-angle (MOC/WA) image overlain with OMEGA phyllosilicate detections and locations of the CRISM images presented. Fe/Mg-smectite was mapped with the band at 2.3 μm (orange), and a combination of Al-phyllosilicate (montmorillonite/kaolinite) and hydrated silica was mapped with the 2.2-μm band (blue). The ~10-km-wide footprints are shown for three targeted CRISM images.

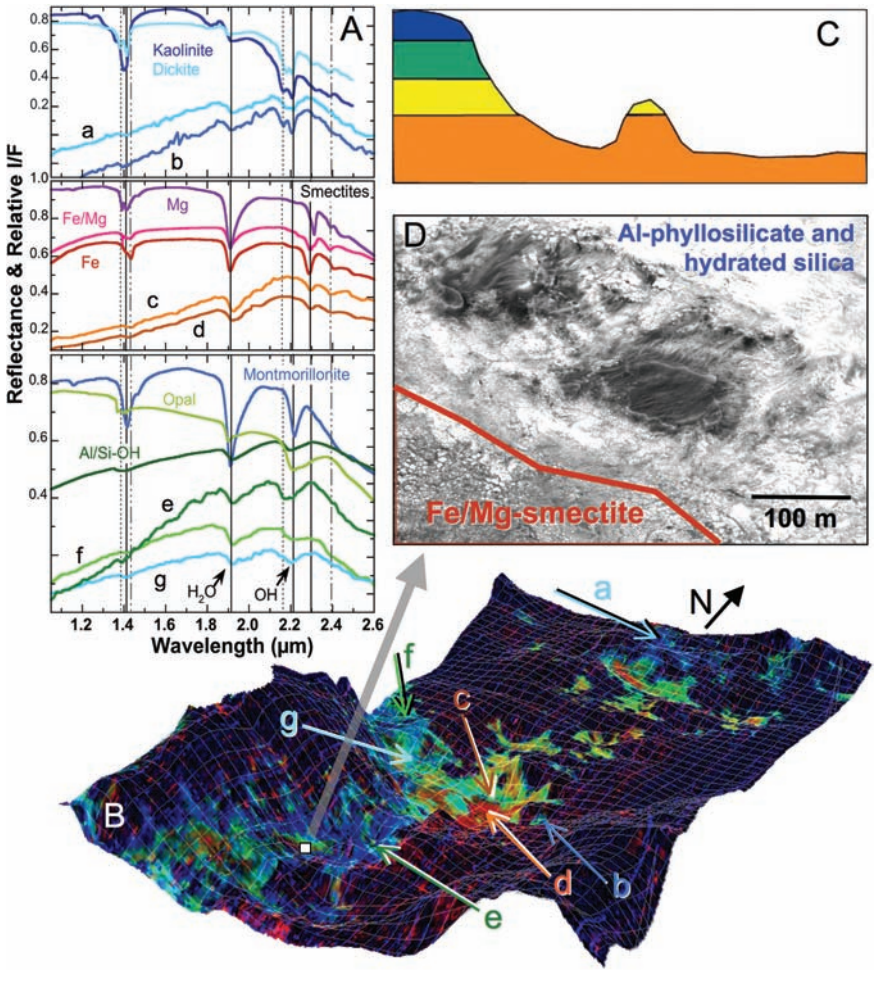

Fig. 2. Phyllosilicate-bearing deposits in western Mawrth Vallis. (**A**) CRISM spectra from image HRL000043EC (and the overlapping image FRT0000863E) compared to lab spectra of phyllosilicates and hydrated silica-bearing materials (*15*, *16*). (**B**) Mineral indicator map draped over MOLA terrain with ×20 vertical enhancement showing Fe/Mg-smectite (orange/red), Al-phyllosilicate and hydrated silica (blue), and Fe^{2+}-bearing phases (yellow/green). (**C**) Sample stratigraphy of phyllosilicates consistent with observations throughout the region, using the colors from (B). (**D**) Portion of HiRISE image PSP_005819_2050_RED, showing the transition from the polygonal Fe/Mg-smectite terrain in the lower left to the scaly Al-phyllosilicate and smooth hydrated silica in the upper right with two dark patches of mafic material.

(Fig. 2A, spectra e and f; Fig. 3A, spectra c and d) are attributed to Al/Si-OH or Si-OH (hydrated silica) (*10*). The Al-phyllosilicate and hydrated silica appear to be intermixed in most places because the sharp 1.41-, 1.91-, and 2.21-μm bands characteristic of montmorillonite are rare, whereas broad bands centered near 1.38, 1.93, and 2.21 μm (observed for opal) or 1.39, 1.92, and 2.19 μm (observed for Al/Si-OH species) are more common.

Observations from the Thermal Emission Spectrometer (with a spatial resolution of 3 to 6 km per pixel) show that the light-toned units are dominated by feldspar and a silica-rich phase (*11*). This silica detection is consistent with the Si-OH and Al/Si-OH bands identified in CRISM spectra here. Feldspar is not directly observable in the VNIR spectral region and could be present as well in the phyllosilicate-bearing rocks.

Additional spectra contain a band at ~1.4 μm and a doublet near 2.2 μm (Fig. 2A, spectra a and b), consistent with the kaolinite family. Many of these spectra also include a weak band near 1.93 μm attributed to bound water in a hydrated component (such as hydrated silica, montmorillonite, or ferrihydrite). A crisp doublet is observed at 2.16 and 2.20 μm (Fig. 2A, spectrum b) in a few cases that resembles kaolinite; in most spectra, a less resolved doublet is present at ~2.18 and 2.20 μm (Fig. 2A, spectrum a) that is more consistent with dickite.

Analyses of spectra collected at Mawrth Vallis in relation to Mars Orbiter Laser Altimeter (MOLA) topography (Figs. 2B and 3, C and D, and movie S1) reveal that Fe/Mg-smectite is prevalent in valley tributaries and other topographic lows (the southern part of the CRISM image in Fig. 3D and the central part of the image in Fig. 3C), whereas the raised knobs (Fig. 3C) and higher-elevation regions (Fig. 3D) contain Al-phyllosilicates. The Fe/Mg-smectite exposures appear to be thicker and more resistant to erosion, and in most areas they are the lowest unit visible. CRISM-MOLA analyses indicate that the Fe/Mg-smectite–rich rocks are typically 200 to 300 m lower in elevation than neighboring Al-phyllosilicate–rich and hydrated silica-rich layers and that the Al-phyllosilicates are probably covering the Fe/Mg-smectites (Fig. 2C). This is consistent with independent analyses of High Resolution Imaging Science Experiment (HiRISE) data (*12*). Many regions bordering the Fe/Mg-smectite–rich rocks (Fig. 3D) yield spectra with features similar to that of hydrated silica, plus a NIR slope that could indicate a ferrous mica such as celadonite or glauconite. However, laboratory spectra of these phyllosilicates also have weak bands near 2.2 to 2.35 μm that are not resolved in the CRISM spectra. A side view of a fissure through the channel wall (Fig. 3C) shows that Al-phyllosilicate–rich rocks lie stratigraphically above the Fe/Mg-smectite unit, which itself covers nonhydrated rocks below.

Units containing Fe/Mg-smectite, montmorillonite/hydrated silica, and kaolinite/hydrated silica exhibit distinct textures in the HiRISE images of this region (*12*). As demonstrated in Fig. 2D, the Fe/Mg-smectite unit exhibits a fractured polygonal surface consistent with the contraction of smectites exposed to dehydration. In contrast, the units containing hydrated silica possess a smooth texture, and those with montmorillonite are characterized by a polygonally fractured texture on a smaller scale than that observed for the Fe/Mg smectites. Kaolinite is observed in alteration regions as small as 50 m across, but in a few cases much larger, and appears to exhibit a smooth texture.

Phyllosilicates have been detected in a number of outcrops of Mars' ancient crust surrounding Mawrth Vallis (*13*), suggesting that the processes forming phyllosilicates here may have been widespread and that only a fraction of the phyllosilicate-rich rocks has been exposed. The initial Fe/Mg-smectite probably formed via aqueous alteration of basalt, the dominant lithology of the Martian highlands (*3*, *14*). This smectite unit appears to drape the topography and exhibits layered textures suggesting that ash was the basaltic precursor. Alteration could have occurred during direct deposition of ash onto an open body of water or by groundwater. Alternative sources include basaltic sediments and impact ejecta. The layering is complex, indicating perhaps multiple depositional events over a prolonged time period (*1*). The specific processes forming the additional clay minerals and stratigraphic relations remain unclear. Subsequent aqueous alteration and leaching of Fe and Mg from the smectite or ash could have produced hydrated silica, montmorillonite, mica, and kaolinite, as could a change in aqueous chemistry (for example, through hydrothermal activity) or alteration of a later Si-rich volcanic ash or sediment. Another possible scenario is the alteration of interbedded source rocks with different chemistries, resulting in changing alteration profiles.

Possible terrestrial analogs for the hydrated silica phases are the opal formed in hydrated ash on the southern rim of the Kilauea caldera (*15*) and hydrated amorphous Al/Si-OH phases formed in altered volcanic material at Haleakala crater in Hawaii (*16*). Acidic conditions and/or hot and humid climates support active hydrolysis and ion leaching that can result in formation of kaolinite and hydrated silica (*17*, *18*). The NIR slope interpreted as an Fe^{2+} phase is unusual because iron typically precipitates out of solution as Fe^{3+} oxides/oxyhydroxides or sulfates and because the Fe^{2+} unit occurs on top of the Fe^{3+} nontronite-like unit.

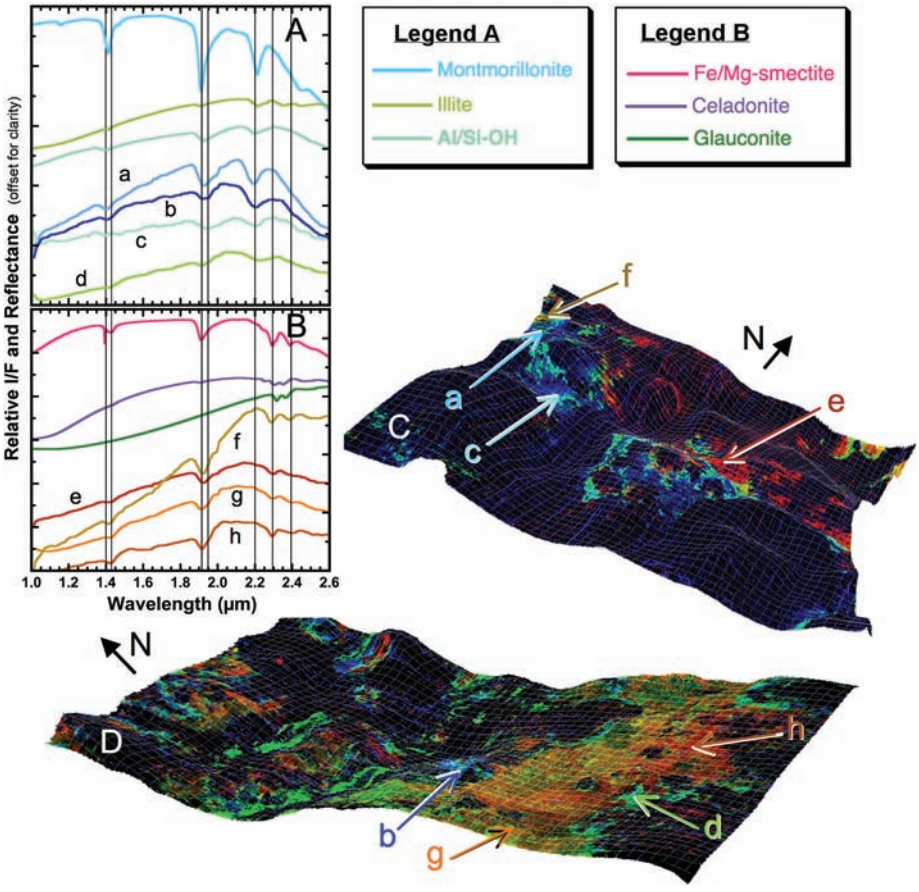

Fig. 3. Phyllosilicate-bearing deposits along the Mawrth Vallis channel. (**A** and **B**) CRISM spectra compared to lab spectra of phyllosilicates and other hydrated phases. (**C** and **D**) Mineral indicator maps of CRISM images FRT00003BFB (C) and HRL0000285A (D) draped over MOLA terrain with ×10 vertical enhancement showing Fe/Mg-smectites (orange/red), Al-phyllosilicates and hydrated silica (blue), and Fe^{2+}-bearing phases (yellow/green).

On Earth, Fe^{3+} is normally converted to Fe^{2+} in aqueous environments by acidophilic bacteria (*19*–*21*). If an Fe^{2+} phase does exist, then a reducing element must have been present at Mawrth Vallis in order to convert the Fe^{3+} to Fe^{2+}, or some form of activity [such as hydrothermal processes (*22*–*24*)] could have reduced the nontronite or released abundant Fe^{2+} in solution that precipitated out before being converted to Fe^{3+}. Thus, the complex and potentially multi-event formation conditions of phyllosilicates at Mawrth Vallis present a fascinating window into past aqueous activity on Mars.

References and Notes

1. J. R. Michalski, E. Z. Noe Dobrea, *Geology* **35**, 951 (2007).
2. S. Murchie *et al.*, *J. Geophys. Res.* **112**, 10.1029/2006JE002682 (2007).
3. See supporting material on *Science* Online.
4. F. Poulet *et al.*, *Nature* **438**, 623 (2005).
5. J.-P. Bibring *et al.*, *Science* **307**, 1576 (2005).
6. D. Loizeau *et al.*, *J. Geophys. Res.* **112**, 10.1029/2006JE002877 (2007).
7. J. F. Mustard *et al.*, *Nature*, 10.1038/nature07097 (2008).
8. J. L. Bishop, E. Murad, M. D. Dyar, *Clay Miner.* **37**, 617 (2002).
9. J. L. Bishop, J. Madejova, P. Komadel, H. Fröschl, *Clay Miner.* **37**, 607 (2002).
10. R. E. Milliken *et al.*, *Geology*, in press.
11. J. R. Michalski *et al.*, paper presented at the 7th International Mars Conference, Pasadena, CA, 2007.
12. J. J. Wray, B. L. Ehlmann, S. Squyres, J. F. Mustard, R. L. Kirk, *Geophys. Res. Lett.*, 10.1029/2008GL034385 (2008).
13. E. Z. Noe Dobrea *et al.*, paper presented at the Lunar and Planetary Science Conference, Lunar and Planetary Institute, Houston, TX, 2008.
14. J. L. Bandfield, V. E. Hamilton, P. R. Christensen, *Science* **287**, 1626 (2000).
15. J. L. Bishop, P. Schiffman, M. D. Lane, M. D. Dyar, paper presented at the Lunar and Planetary Science Conference, Lunar and Planetary Institute, Houston, TX, 2005.
16. J. L. Bishop *et al.*, *Clays Clay Miner.* **55**, 1 (2007).
17. H. Chamley, *Clay Sedimentology* (Springer-Verlag, New York, 1989).
18. M. L. Jackson, *Clays Clay Miner.* **6**, 133 (1957).
19. H. A. Lowenstam, *Science* **211**, 1126 (1981).
20. K. H. Nealson, *Annu. Rev. Earth Planet. Sci.* **25**, 403 (1997).
21. T. D. Brock, J. Gustafson, *Appl. Environ. Microbiol.* **32**, 567 (1976).
22. M. J. Nelson, H. E. Newsom, D. S. Draper, *Geochim. Cosmochim. Acta* **69**, 2701 (2005).
23. J. W. Stucki, D. Tessier, *Clays Clay Miner.* **39**, 137 (1991).
24. P. R. L. Browne, *Annu. Rev. Earth Planet. Sci.* **6**, 229 (1978).

25. The authors thank E. Cloutis and an anonymous reviewer for helpful editorial comments and the CRISM Science Team for acquisition of the images. Supported by NASA's Mars Reconnaissance Orbiter project, Mars Data Analysis program, Mars Fundamental Research program, and the NASA Astrobiology Institute.

Supporting Online Material

www.sciencemag.org/cgi/content/full/321/5890/830/DC1
Materials and Methods
Table S1
References
Movie S1

28 April 2008; accepted 17 June 2008
10.1126/science.1159699

Brown Carbon Spheres in East Asian Outflow and Their Optical Properties

Duncan T. L. Alexander,[1] Peter A. Crozier,[2]* James R. Anderson[3]

Atmospheric aerosols play a substantial role in climate change through radiative forcing. Combustion-produced carbonaceous particles are the main light-absorbing aerosols; thus, quantifying their optical properties is essential for determining the magnitude of direct forcing. By using the electron energy-loss spectrum in the transmission electron microscope, we quantified the optical properties of individual, submicrometer amorphous carbon spheres that are ubiquitous in East Asian–Pacific outflow. The data indicate that these common spheres are brown, not black, with a mean refractive index of $1.67 - 0.27i$ (where $i = \sqrt{1}$) at a wavelength of 550 nanometers. The results suggest that brown carbon aerosols should be explicitly included in radiative forcing models.

The importance of the impact of tropospheric aerosols on Earth's radiative balance and the uncertainty associated with radiative forcing due to aerosols are now well established by the large body of research summarized in the reports from the Intergovernmental Panel on Climate Change (*1*, *2*). A substantial fraction of the anthropogenic aerosol mass is in the form of carbonaceous particles arising from fossil fuel and biomass burning. (Carbonaceous aerosols also derive from natural biogenic emissions.) Most direct radiative forcing models classify carbonaceous particles into two main components, consisting of either negligibly absorbing organic carbon or strongly absorbing black carbon (*1*, *2*). Optical properties are incorporated through the inclusion of model parameters that account mainly for the size distribution and refractive indices of the particles.

Aside from the problem of choosing suitable refractive indices for both forms of carbon from the wide range of values found in the literature (*3*–*11*), this approach ignores the possibility of rich variations in the refractive indices of carbon arising from both changes in emission source and changes during transport in the atmosphere. To improve the accuracy of direct forcing models, it is necessary to have more precise information on the size, shape, composition, mixing state, and refractive indices of individual carbonaceous aerosols. It is difficult to determine these parameters from light-optical measurements alone because the signals are averaged over all aerosol components (size, composition, structure; see fig. S1).

We used a transmission electron microscopy (TEM) method to identify the optical properties of individual particles in ambient aerosols. We applied this method to the highly abundant carbon spheres found in all examined samples of ambient aerosols collected above the Yellow Sea during the Asian Pacific Regional Aerosol Characterization Experiment (ACE-Asia) (*12*); bulk optical properties, scanning electron microscopy images of samples taken simultaneously

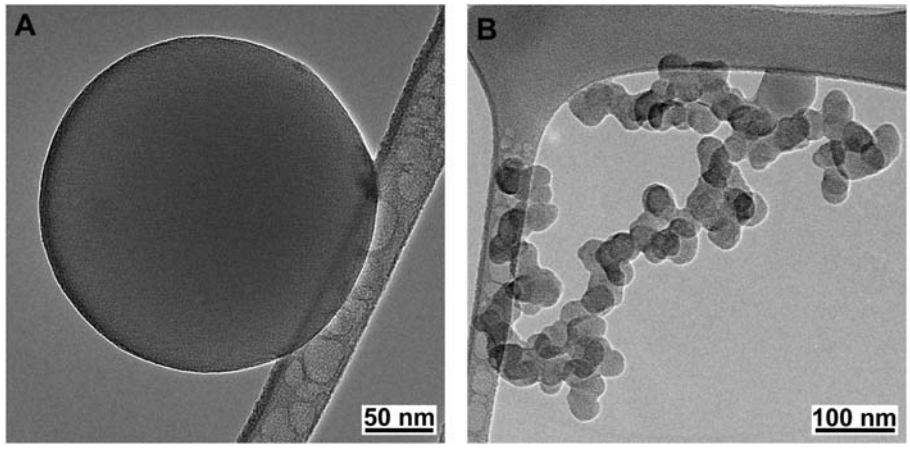

Fig. 1. A bright-field TEM image of a typical amorphous carbon sphere (**A**) and a soot carbon particle (**B**) from the atmospheric aerosol sampled at an altitude of 30 m during flight 13 of ACE-Asia.

[1]LeRoy Eyring Center for Solid State Science, Arizona State University, Post Office Box 871704, Tempe, AZ 85287, USA. [2]School of Materials, Arizona State University, Post Office Box 878706, Tempe, AZ 85287, USA. [3]Department of Mechanical and Aerospace Engineering, Arizona State University, Post Office Box 876106, Tempe, AZ 85287, USA.

*To whom correspondence should be addressed. E-mail: crozier@asi.edu